

Identification of electrostatic microinstability maps in quasi-axisymmetric stellarator

Cite as: Phys. Plasmas **29**, 052505 (2022); <https://doi.org/10.1063/5.0082107>

Submitted: 12 December 2021 • Accepted: 19 April 2022 • Published Online: 11 May 2022

 J. Huang, M. Nakata,  Y. Xu, et al.



View Online



Export Citation



CrossMark



Physics of Plasmas
Features in Plasma Physics Webinars

Register Today!



Identification of electrostatic microinstability maps in quasi-axisymmetric stellarator

Cite as: Phys. Plasmas **29**, 052505 (2022); doi: [10.1063/5.0082107](https://doi.org/10.1063/5.0082107)

Submitted: 12 December 2021 · Accepted: 19 April 2022 ·

Published Online: 11 May 2022



View Online



Export Citation



CrossMark

J. Huang,^{1,a)} M. Nakata,^{2,3,4} Y. Xu,^{1,a)} A. Shimizu,^{2,3} M. Isobe,^{2,3} S. Okamura,² H. F. Liu,¹ X. Q. Wang,¹ X. Zhang,¹ H. Liu,¹ J. Cheng,¹ and C. J. Tang^{1,5}

AFFILIATIONS

¹Institute of Fusion Science, School of Physical Science and Technology, Southwest Jiaotong University, Chengdu 610031, China

²National Institute for Fusion Science, National Institutes of Natural Sciences, Toki 509-5292, Japan

³The Graduate University for Advanced Studies, SOKENDAI, Toki 509-5292, Japan

⁴PRESTO, Japan Science and Technology Agency, 418, Honcho, Kawaguchishi, Saitama 332-0012, Japan

⁵College of Physics, Sichuan University, Chengdu 610064, China

^{a)}Authors to whom correspondence should be addressed: jiehuang@swjtu.edu.cn and xuyuhong@swjtu.edu.cn

ABSTRACT

Microinstabilities such as ion temperature gradient (ITG) mode and trapped electron mode (TEM) in quasi-axisymmetric (QA) stellarator are investigated by using gyrokinetic Vlasov simulations, where the QA configuration of Chinese first quasi-axisymmetric stellarator is utilized. Extensive parameter scans with respect to the density and temperature gradients for the zero beta cases identify the microinstability maps that indicate the transition boundary among ITG and TEM. It is found that, in particular for the modes with the ion-gyroradius scale, a relatively more stabilized regime appears along the transition boundary of ITG–TEM. Such a valley-like stability structure is not observed in the other cases with the sub-ion-gyroradius-scale. A stabilization effect attributed to the hollow density profile is also demonstrated.

Published under an exclusive license by AIP Publishing. <https://doi.org/10.1063/5.0082107>

I. INTRODUCTION

In most tokamaks, the energy and particle transport is mainly caused by turbulence, which is driven by the microinstabilities such as the ion temperature gradient mode (ITG) and trapped electron mode (TEM) in the ion gyroradius scale. In addition to the turbulent transport, the neoclassical transport also has a large contribution in traditional stellarators.¹ In order to suppress the neoclassical transport, several optimization concepts are proposed to enhance the confinement in stellarators.^{2–5} One of the concepts is so-called quasi-axisymmetric (QA) stellarator.^{6,7} The QA stellarator is an optimized non-axisymmetric plasma with a nearly axisymmetric magnetic field strength, and the neoclassical transport is reduced almost to the level of tokamaks.⁸ It is considered that the QA stellarator is not a hybrid device of tokamak and stellarator, either, but it combines advantageous points from both tokamak and stellarator, where several QA devices have been designed, such as CHS-qa in Japan⁹ and National Compact Stellarator Experiment (NCSX) in United States.^{5,10} So far, there has been no realistic devices of QA stellarator in the world, but now Chinese first quasi-axisymmetric stellarator (CFQS) is being built in Southwest Jiaotong

University (SWJTU) in China, under a joint project between SWJTU and National Institute for Fusion Science (NIFS) in Japan.^{8,11–14}

Although theoretical analyses show that the neoclassical transport in QA stellarators is small, the microinstabilities and the resultant turbulent transport still remained to clarify. Therefore, it is important to examine how such QA optimization affects the properties of microinstabilities and turbulent transport, which is usually thought to be associated with the ITG, TEM, and so on.¹⁵ The stabilization effects of three-dimensional geometry on the microinstability have been studied,^{16–18} and several works on the gyrokinetic analyses of microinstabilities in the QA stellarator, especially for NCSX, have been done.^{19–21} However, an overall structure of the microinstabilities on the parameter space has not been identified in the previous studies.

In this paper, the gyrokinetic Vlasov code GKV is used to investigate the ITG and TEM in CFQS, including the nature of the microinstability map. The rest of the paper is organized as follows. In Sec. II, the gyrokinetic Vlasov simulation model and settings are briefly introduced. The simulation results are shown in Sec. III. Finally, the conclusions are given in Sec. IV.

II. GYROKINETIC VLASOV SIMULATION MODEL AND NUMERICAL SETTINGS

Electrostatic microinstabilities in a QA stellarator are investigated by means of a gyrokinetic Vlasov simulation code GKV.^{22–24} The GKV code is based on the so-called δf gyrokinetic model and solves time evolution of perturbed distribution functions δf_s of ions ($s = i$) and electrons ($s = e$), the electrostatic potential ϕ , and the parallel component of the vector potential A_{\parallel} . The governing equation is the electromagnetic gyrokinetic equation for the perturbed distribution functions δf_s on the five dimensional phase space $(\mathbf{x}_g, v_{\parallel}, \mu)$.^{25,26} The Fourier representation with the perpendicular wavenumber \mathbf{k}_{\perp} is given by

$$\begin{aligned} & \left(\frac{\partial}{\partial t} + v_{\parallel} \mathbf{b} \cdot \nabla + i\omega_{Ds} - \frac{\mu \mathbf{b} \cdot \nabla B}{m_s} \frac{\partial}{\partial v_{\parallel}} \right) \delta g_{s\mathbf{k}_{\perp}} \\ & - \frac{c}{B} \sum_{\Delta} \mathbf{b} \cdot (\mathbf{k}_{\perp}' \times \mathbf{k}_{\perp}'') \delta \psi_{s\mathbf{k}_{\perp}'} \delta g_{s\mathbf{k}_{\perp}''} \\ & = \frac{e_s F_{Ms}}{T_s} \left(\frac{\partial \delta \psi_{\mathbf{k}_{\perp}}}{\partial t} + i\omega_{*Ts} \delta \psi_{\mathbf{k}_{\perp}} \right) + C_s(\delta g_{s\mathbf{k}_{\perp}}), \end{aligned} \quad (1)$$

where $\delta g_{s\mathbf{k}_{\perp}}$ stands for the non-adiabatic part or the kinetic part of the perturbed distribution functions $\delta f_{s\mathbf{k}_{\perp}}$ in the Fourier form with the perpendicular wavenumber \mathbf{k}_{\perp} , i.e., $\delta g_{s\mathbf{k}_{\perp}} = \delta f_{s\mathbf{k}_{\perp}} + e_s J_0 \delta \phi_{\mathbf{k}_{\perp}} F_{Ms}/T_s$. J_0 is the zeroth-order Bessel function and represents the finite gyroradius effect. F_{Ms} is the equilibrium part of the distribution function given by the local Maxwellian distribution. The second term on the left hand is the nonlinear term, and the symbol Σ_{Δ} means the double summations with respect to \mathbf{k}_{\perp}' and \mathbf{k}_{\perp}'' , which satisfy the triad-interaction condition of $\mathbf{k}_{\perp} = \mathbf{k}_{\perp}' + \mathbf{k}_{\perp}''$. ω_{Ds} and ω_{*Ts} are the magnetic and diamagnetic drift frequencies, respectively. $\delta \psi_{\mathbf{k}_{\perp}}$ is the gyro-averaged potential fluctuation. In GKV, collisional effects are introduced in terms of a linearized model collision operator C_s , where a gyro-averaged Lenard–Bernstein model is applied,²⁷ and the collisional effects are discussed in, e.g., Ref. 28.

In GKV, a local flux-tube coordinate (x, y, z) ,²⁹ which is defined as $x = a(\rho - \rho_0)$, $y = a\rho_0/q(\rho_0)[q(\rho)\theta - \zeta]$, $z = \theta$ based on the straight field-line coordinates (ρ, θ, ζ) , is applied, where a is the minor radius, $\rho = \sqrt{\psi/\psi_{\text{edge}}}$ with the toroidal flux ψ , and $q(\rho_0)$ is the safety factor on the flux surface with $\rho = \rho_0$.

In the simulations, we use a standard CFQS equilibrium generated by the variational moments equilibrium code (VMEC).³⁰ The magnetic configuration of CFQS is quasi-axisymmetric with two magnetic field periods, and the aspect ratio is 4, and the major radius is 1 m. The shape of the poloidal cross section of the CFQS configuration varies with the toroidal angles.^{8,11} A zero-beta vacuum magnetic equilibrium is considered, and the following simulations look into a local position at $\rho = 0.5$, where the field line label of $\alpha = \zeta - q(\rho)\theta = 0$ is fixed. Beta is the ratio of the reference pressure to the reference magnetic energy density, i.e., $\beta = \mu_0 n_{\text{ref}} T_{\text{ref}}/B_{\text{ref}}^2$. The wave number $k_y \rho_i$ is taken as 0.05, 0.01, ..., 2.5, where the radial wavenumber k_x is set to be zero. The grid number along the field line (z -direction) is 1536 for six poloidal turns, and 60 and 16 grid numbers are used for v_{\parallel} and μ directions with the maximum of 4 v_{ti} , respectively. Also, $T_i/T_e = 1$. Figure 1 shows the variation of the magnetic field intensity along the field line of a poloidal turn.

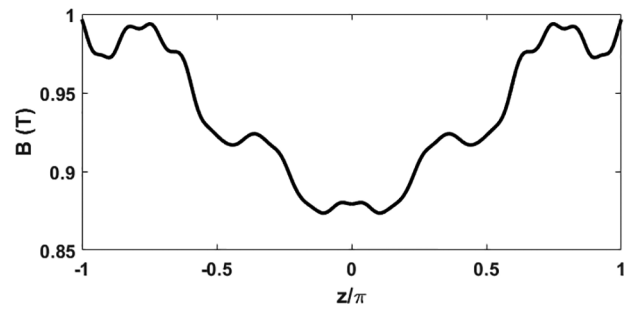


FIG. 1. The magnetic field intensity along the field line at $\rho = 0.5$ and $\alpha = 0$ for CFQS.

III. SIMULATION RESULTS

A. Electrostatic ITG modes with adiabatic electrons

If the kinetic part of the perturbed distribution function of electron is ignored, the trapped electron effect is not included in the simulation model. The adiabatic electron approximation is still useful because one can see the fundamental properties of the electrostatic ITG mode, where the parametric dependence of the ITG modes is examined.

Figure 2 shows the growth rate spectrum of electrostatic adiabatic ITG for different temperature gradients R_0/L_T at density gradient $R_0/L_n = 0$. From Fig. 2, there is a critical temperature gradient for ITG. If R_0/L_T exceeds this critical gradient, ITG modes are destabilized and the growth rate increases with the increase in R_0/L_T . This tendency is also found in tokamaks and other stellarators.³¹ Figure 3 shows R_0/L_T dependence of the maximum growth rates for the different values of the density gradient R_0/L_n . One finds a variation of the critical temperature gradient depending on the density gradient. The growth rate increases almost linearly with R_0/L_T for any R_0/L_n . By fitting these lines, the threshold of the critical temperature gradient for ITG modes is estimated. A negative R_0/L_n enhances this threshold, and a positive R_0/L_n can reduce the threshold first and then enhances it as R_0/L_n increases. The critical gradient of $R_0/L_n = 0$ is $R_0/L_{T,\text{crit}} \approx 3.37$ for CFQS. When the value is compared to that in previously evaluated

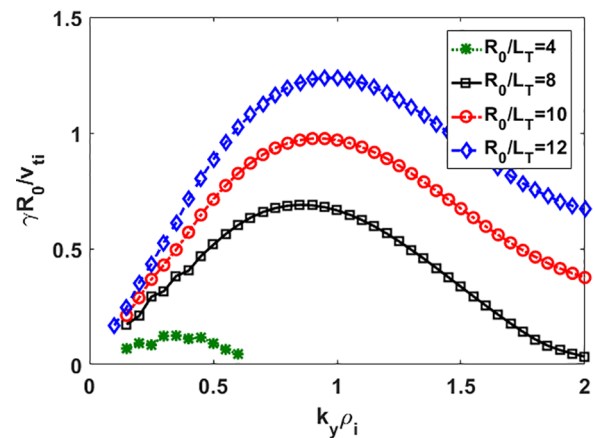


FIG. 2. The growth rates of electrostatic adiabatic ITG modes vs $k_y \rho_i$ for various R_0/L_T at $R_0/L_n = 0$.

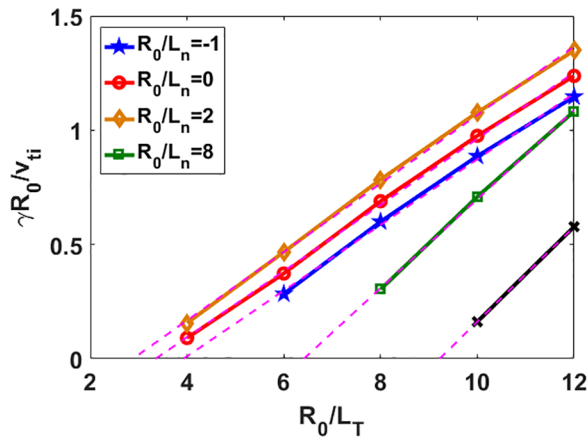


FIG. 3. The maximum growth rates of electrostatic adiabatic ITG modes vs R_0/L_T for various R_0/L_n . The dashed lines are the fitted lines of the curves.

critical gradient of $R_0/L_{T,crit} \approx 3.51$ for NCSX, we see a similar critical gradient, where the $R_0/L_{T,crit}$ is re-calculated from $a_N/L_{T,crit} \approx 1.13$ with the minor radius of $a_N \approx 0.322$ m in NCSX.¹⁹ The comparison of the CFQS and NCSX results indicates that the fundamental adiabatic ITG modes are quite weakly affected by the difference of the magnetic geometry between the CFQS and NCSX.

The impact of the density gradient on the ITG mode growth rate is highlighted in Fig. 4. It is found that the growth tends to be reduced toward the largely positive R_0/L_n . Moreover, in the case with negative R_0/L_n , i.e., a hollow density profile, the reduction in the ITG mode growth rate is revealed. Such a non-monotonic relationship between the growth rate and R_0/L_n has also been found in the tokamak case.³²

B. Electrostatic microinstabilities with kinetic electrons

Kinetic electrons are the key factor for triggering TEMs, and they also can affect ITG modes. In the cases with kinetic electrons, ITG

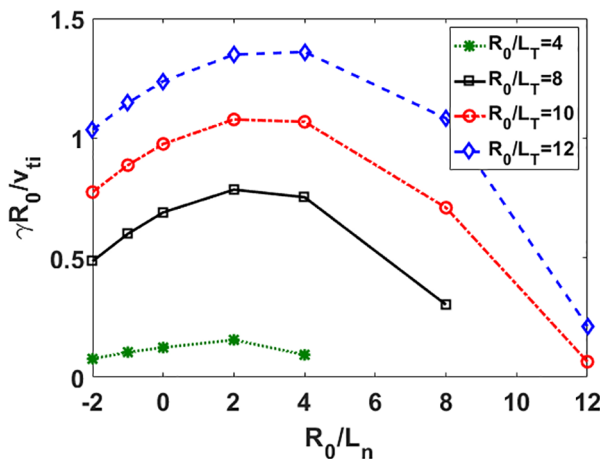


FIG. 4. The maximum growth rates of electrostatic adiabatic ITG modes vs R_0/L_n for various R_0/L_T .

modes and TEMs can coexist. In this subsection, we examine such electrostatic kinetic ITG-TEM modes in CFQS. Note that the trapped electron effect is excluded in the simulation model when the kinetic response of the perturbed distribution function of electrons is ignored. This is the so-called adiabatic electron approximation, and such treatment is still useful for studies of the pure ITG mode and for the cross-code benchmark. The simulation results about the ITG mode in the adiabatic electron approximation are shown in the Appendix.

Figure 5 shows the growth rate and the real frequency spectrum for various R_0/L_T at $R_0/L_n = 0$, where R_0 is the major radius, and $L_T = -(d \ln T_s / dx)^{-1}$. Here, $R_0/L_{Ti} = R_0/L_{Te}$ is assumed. The growth rate γ and the real frequency ω are normalized to v_{ti}/R_0 , where v_{ti} is the ion thermal velocity. From Fig. 5(a), the transition from ITG mode to TEM with the frequency switch is found, and the discontinuities in ω and γ appear near the transition wavenumber. Note that the propagating directions of the ITG mode and TEM are the ion diamagnetic (the negative real frequency) and the electron diamagnetic drift directions (the positive real frequency), respectively. To compare with the adiabatic results shown in Fig. 2, kinetic electrons yield a higher growth rate of the ITG mode. One can see that the growth rates of TEM are also proportional to R_0/L_T , but this is attributed mainly to the electron temperature gradient (cf. $T_i/T_e = 1$).

Figure 6 shows the density and temperature gradient dependence of the growth rates and real frequencies for the hybrid ITG-TEM modes at fixed $k_y \rho_i$. We recognize that the dominant mode at $k_y \rho_i = 1$ is the ITG mode with the negative frequency and the dominant mode at $k_y \rho_i = 2.5$ is the TEM with the positive frequency. In the adiabatic case, both a negative density gradient and a large density gradient can suppress ITG modes, seen in Figs. 3 and 6(a). Similarly, in the kinetic case, a large density gradient, i.e., $R_0/L_n > 4$, can suppress ITG modes, seen in Figs. 6 and 7. Therefore, when $R_0/L_T < 8$ and $R_0/L_n > 4$, the dominant mode is TEM. On the other hand, for $k_y \rho_i = 2.5$, this is smaller than the ion scale and the dominant mode is the TEM, seen in Fig. 6(b). It is found that a density profile with a negative gradient, blue case in Fig. 6(b), is not useful to suppress the TEM. Figure 7 displays similar results, but the horizontal axis is converted from the temperature gradient to the density gradient in order to highlight the stabilization effects by the density gradient. It is clearly shown that the ITG modes can be suppressed by a density profile with a negative gradient, seen in the green and pink cases in Fig. 7(a). Such ITG stabilization by a hollow density profile has not been reported in the gyrokinetic analysis for QA stellarators. For high R_0/L_T cases, a similar tendency is observed for the TEM modes. These results suggest that, in the CFQS configuration, the hybrid ITG-TEM modes can be suppressed when the absolute value of R_0/L_n is enough large even at some large value of R_0/L_T .

The previous results are given by setting $R_0/L_{Ti} = R_0/L_{Te}$ in the simulations. However in experiments, the electron temperature is easily changed by electron cyclotron resonance heating, which causes a different value of ion temperature gradient and electron temperature gradient. In order to study such an effect of the different heating scenario on hybrid ITG-TEM instabilities, the cases with a fixed electron temperature gradient are simulated here. Because the typical R_0/L_{Te} in CFQS has not been known yet, the electron temperature gradient is set as $R_0/L_{Te} = 8$, which is the typical value in the other devices like the large helical device. Figure 8 shows the growth rate spectrum and the real frequency spectrum of the hybrid ITG-TEM modes for

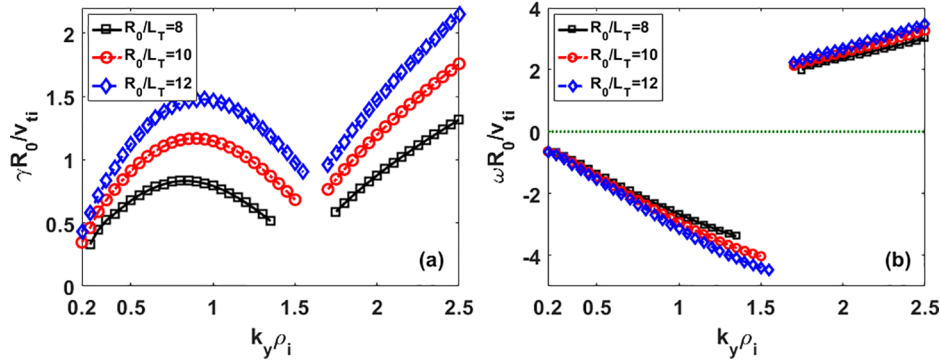


FIG. 5. The growth rates (a) and real frequencies (b) of the hybrid ITG-TEM modes vs $k_y \rho_i$ for various R_0/L_T at $R_0/L_n = 0$. Here, $R_0/L_{Ti} = R_0/L_{Te}$.

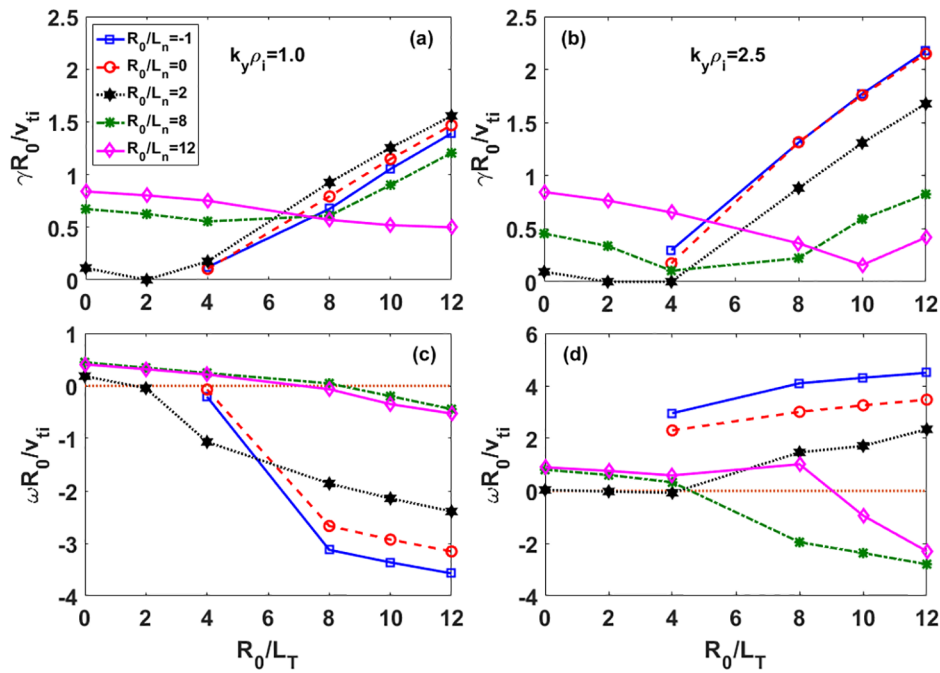


FIG. 6. The growth rates and real frequencies of the electrostatic hybrid ITG-TEM modes vs R_0/L_T for several values of R_0/L_n at (a) and (c) $k_y \rho_i = 1.0$ and (b) and (d) $k_y \rho_i = 2.5$.

$R_0/L_{Te} = 8$ and $R_0/L_n = 0$. When $R_0/L_{Ti} \leq 4$, the dominant instability is TEM. This is due to a large electron temperature gradient to drive a strong TEM, and $R_0/L_{Ti} \leq 4$ is not large enough to drive a strong ITG mode. As R_0/L_{Ti} increases, ITG modes become more pronounced and dominate in the low $k_y \rho_i$ region. It is also found that R_0/L_{Ti} can suppress TEMs.^{28,33}

Figure 9 shows the stability contour map of the growth rates of the electrostatic hybrid ITG-TEM modes with $k_y \rho_i = 1.0, 2.5$ vs R_0/L_n and R_0/L_{Ti} for $R_0/L_{Te} = 8$. For $k_y \rho_i = 1.0$, a small density gradient or a larger density gradient can suppress ITG mode, and the density gradient can drive TEM. Therefore, the top left of Fig. 9(a) is dominated by ITG and the bottom right is dominated by TEM. It is found that a stability-valley-like structure appears along the transition boundary of the ITG and TEM with $R_0/L_n \approx R_0/L_{Ti}$, where the growth rate is relatively low. A similar structure has also been found in the gyrokinetic analysis for the W7-X.³⁴ On the other hand, for

$k_y \rho_i = 2.5$, the most unstable TEM is located in the region where both R_0/L_n and R_0/L_{Ti} are nearly zero. Then, one can see a significant descent of the TEM growth rate toward the transition boundary for the ITG modes. Hence, the valley-like structure no longer appears for the case in higher wavenumber.

IV. CONCLUSIONS AND DISCUSSION

The electrostatic microinstabilities such as ITG and TEM in the QA stellarator CFQS are investigated by using the gyrokinetic Vlasov code GKV, and their global stability characteristics are identified.

Considering the kinetic electrons in the model, the kinetic hybrid ITG-TEM modes can be examined. In the low $k_y \rho_i$ region, the dominant mode is ITG. In the high $k_y \rho_i$ region, the dominant mode is TEM. Such hybrid ITG-TEM modes can be suppressed when the absolute value of R_0/L_n is enough large even at a some large R_0/L_T . Considering that the ion and electron temperature gradients in

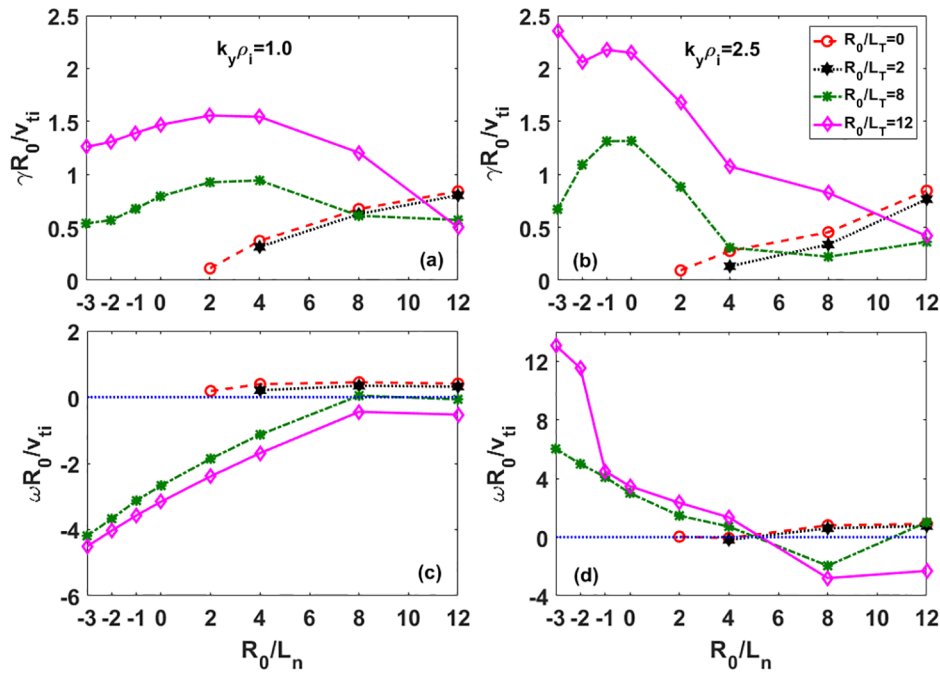


FIG. 7. The growth rates and real frequencies of the electrostatic hybrid ITG-TEM modes vs R_0/L_n for various R_0/L_{Ti} at (a) and (c) $k_y \rho_i = 1.0$ and (b) and (d) $k_y \rho_i = 2.5$.

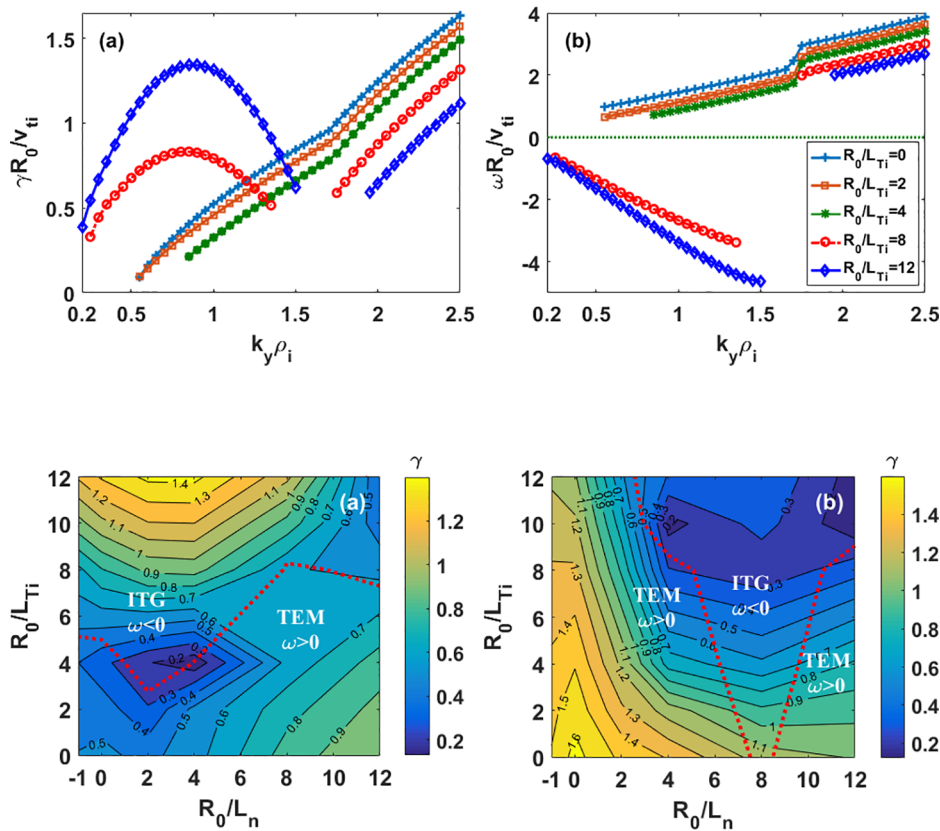


FIG. 8. The growth rates (a) and real frequencies (b) of the hybrid ITG-TEM modes vs $k_y \rho_i$ for various R_0/L_{Ti} at $R_0/L_n = 0$ and $R_0/L_{Te} = 8$.

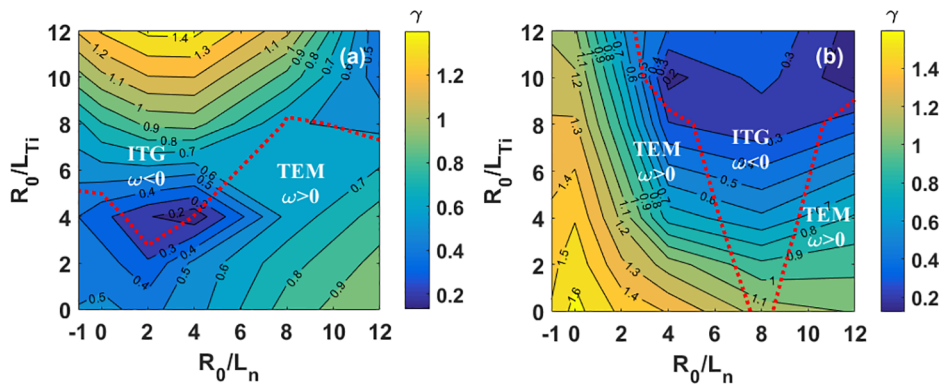


FIG. 9. The stability contour map of the growth rates of the electrostatic hybrid ITG-TEM modes vs R_0/L_n and R_0/L_{Ti} for $R_0/L_{Te} = 8$ at (a) $k_y \rho_i = 1.0$ and (b) $k_y \rho_i = 2.5$. The red dashed line is the boundary of ITG mode dominant region and TEM dominant region.

experiments are generally not equal, the kinetic hybrid ITG-TEM modes for the cases with different R_0/L_{Ti} and R_0/L_{Te} are investigated. Since $R_0/L_{Te} = 8$ is enough to drive a TEM, the TEM is always unstable and becomes dominant when R_0/L_{Ti} is small. As R_0/L_{Ti} increases, the growth rate of TEM decreases and the growth rate of ITG mode increases. A highlighted finding is that a stability-valley-like structure appears along the transition boundary of the ITG and TEM in the stability map for the ion-scale modes. However for the electron-scale modes, there is no this stability-valley-like structure.

In this paper, the field line label of α is set a 0, i.e., toroidal angle $\Phi = 0^\circ$. The flux-tubes with different initial toroidal angles in CFQS have different geometries. The structures along the magnetic field lines at different toroidal angles for the magnetic field intensity and the squared perpendicular wavenumber are different. Because the perpendicular wavenumber is the smallest for $\Phi = 0^\circ$ near $\theta = 0^\circ$, the growth rate of ITG at $\Phi = 0^\circ$ is the largest.¹⁹ The growth rate decreases with the toroidal angle in the half toroidal period for CFQS.

ACKNOWLEDGMENTS

Numerical simulations were performed by Plasma simulator at National Institute for Fusion Science. This work was supported by the National Natural Science Foundation of China through Grant Nos. 11820101004 and 11975188, the National Key R&D Program of China under Grant Nos. 2022YFE03070000, 2022YFE03070001, and 2017YFE0301101 the Sichuan International Science and Technology Innovation Cooperation Project under Grant No. 2021YFH0066, and Central Government Funds of Guiding Local Scientific and Technological Development for Sichuan Province through Grant No. 2021ZYD0024. This work was also supported in part by the general collaboration research program of the National Institute for Fusion Science through the Grant No. NIFS19KBAP051, and in part by “PLADyS,” The Japan Society for the Promotion of Science Core-to-Core Program, A. Advanced Research Networks. This work is also supported in part by Japan Science and Technology Corporation, Precursory Research for Embryonic Science and Technology Grant No. JPMJPR21O7, Japan.

AUTHOR DECLARATIONS

Conflict of Interest

The authors have no conflicts to disclose.

DATA AVAILABILITY

The data that support the findings of this study are available from the corresponding authors upon reasonable request.

REFERENCES

- Y. Xu, *Matter Radiat. Extremes* **1**, 192 (2016).
- H. Yamada, A. Komori, N. Ohyabu, O. Kaneko, K. Kawahata, K. Y. Watanabe, S. Sakakibara, S. Murakami, K. Ida, R. Sakamoto, Y. Liang, J. Miyazawa, K. Tanaka, Y. Narushima, S. Morita, S. Masuzaki, T. Morisaki, N. Ashikawa, L. R. Baylor, W. A. Cooper, M. Emoto, P. W. Fisher, H. Funaba, M. Goto, H. Idei, K. Ikeda, S. Inagaki, N. Inoue, M. Isobe, K. Khlopenkov, T. Kobuchi, A. Kostrioukov, S. Kubo, T. Kuroda, R. Kumazawa, T. Minami, S. Muto, T. Mutoh, Y. Nagayama, N. Nakajima, Y. Nakamura, H. Nakanishi, K. Narihara, K. Nishimura, N. Noda, T. Notake, S. Ohdachi, Y. Oka, M. Osakabe, T. Ozaki, B. J. Peterson, G. Rewoldt, A. Sagara, K. Saito, H. Sasao, M. Sasao, K. Sato, M. Sato, T. Seki, H. Sugama, T. Shimoizuma, M. Shoji, H. Suzuki, Y. Takeiri, N. Tamura, K. Toi, T. Tokuzawa, Y. Torii, K. Tsumori, T. Watanabe, I. Yamada, S. Yamamoto, M. Yokoyama, Y. Yoshimura, T. Watari, Y. Xu, K. Itoh, K. Matsuoka, K. Ohkubo, T. Satow, S. Sudo, T. Uda, K. Yamazaki, O. Motojima, and M. Fujiwara, *Plasma Phys. Controlled Fusion* **43**, A55 (2001).
- A. Dinklage, C. D. Beidler, P. Helander, G. Fuchert, H. Maaßberg, K. Rahbarnia, T. Sunn Pedersen, Y. Turkin, R. C. Wolf, A. Alonso, T. Andreeva, B. Blackwell, S. Bozhakov, B. Buttenschön, A. Czarnecka, F. Effenberg, Y. Feng, J. Geiger, M. Hirsch, U. Höfel, M. Jakubowski, T. Klinger, J. Knauer, G. Kocsis, A. Krämer-Flecken, M. Kubowska, A. Langenberg, H. P. Laqua, N. Marushchenko, A. Mollén, U. Neuner, H. Niemann, E. Pasch, N. Pablant, L. Rudischhauser, H. M. Smith, O. Schmitz, T. Stange, T. Szepesi, G. Weir, T. Windisch, G. A. Wurden, D. Zhang, and W7-X Team, *Nat. Phys.* **14**, 855 (2018).
- J. M. Canik, D. T. Anderson, F. S. B. Anderson, K. M. Likin, J. N. Talmadge, and K. Zhai, *Phys. Rev. Lett.* **98**, 085002 (2007).
- M. C. Zarnstorff, L. A. Berry, A. Brooks, E. Fredrickson, G. Y. Fu, S. Hirshman, S. Hudson, L. P. Ku, E. Lazarus, D. Mikkelsen, D. Monticello, G. H. Neilson, N. Pomphrey, A. Reiman, D. Spong, D. Strickler, A. Boozer, W. A. Cooper, R. Goldston, R. Hatcher, M. Isaev, C. Kessel, J. Lewandowski, J. F. Lyon, P. Merkel, H. Mynick, B. E. Nelson, C. Nuehrenberg, M. Redi, W. Reiersen, P. Rutherford, R. Sanchez, J. Schmidt, and R. B. White, *Plasma Phys. Controlled Fusion* **43**, A237 (2001).
- J. Nührenberg, W. Lotz, and S. Gori, in *Proceedings of the Joint Varenna—Lausanne International Workshop on Theory of Fusion Plasmas*, edited by E. Sindoni and J. Vaclavik (Editrice Compositori, Bologna, 1994), p. 3.
- P. Garabedian, *Phys. Plasmas* **3**, 2483 (1996).
- A. Shimizu, H. F. Liu, M. Isobe, S. Okamura, S. Nishimura, C. Suzuki, Y. Xu, X. Zhang, B. Liu, J. Huang, X. Q. Wang, H. Liu, C. J. Tang, and CFQS Team, *Plasma Fusion Res.* **13**, 3403123 (2018).
- S. Okamura, K. Matsuoka, S. Nishimura, M. Isobe, I. Nomura, C. Suzuki, A. Shimizu, S. Murakami, N. Nakajima, M. Yokoyama, A. Fujisawa, K. Ida, K. Itoh, P. Merkel, M. Drevlak, R. Zille, S. Gori, and J. Nührenberg, *Nucl. Fusion* **41**, 1865 (2001).
- L. E. Dudek, J. H. Chrzanowski, P. J. Heitzenroeder, S. Raftopoulos, M. E. Viola, G. H. Neilson, D. Rej, M. J. Cole, P. Goranson, and K. Freudenberg, *Fusion Eng. Des.* **84**, 351 (2009).
- H. F. Liu, A. Shimizu, M. Isobe, S. Okamura, S. Nishimura, C. Suzuki, Y. Xu, X. Zhang, B. Liu, J. Huang, X. Q. Wang, H. Liu, C. J. Tang, D. P. Yin, Y. Wan, and CFQS Team, *Plasma Fusion Res.* **13**, 3405067 (2018).
- M. Isobe, A. Shimizu, H. F. Liu, H. Liu, G. Z. Xiong, D. P. Yin, K. Ogawa, Y. Yoshimura, M. Nakata, S. Kinoshita, S. Okamura, C. J. tang, Y. Xu, and CFQS Team, *Plasma Fusion Res.* **14**, 3402074 (2019).
- H. F. Liu, A. Shimizu, Y. Xu, S. Okamura, S. Kinoshita, M. Isobe, Y. B. Li, G. Z. Xiong, X. Q. Wang, J. Huang, J. Cheng, H. Liu, X. Zhang, D. P. Yin, Y. Wang, T. Murase, S. Nakagawa, and C. J. Tang, *Nucl. Fusion* **61**, 016014 (2021).
- X. Q. Wang, Y. Xu, A. Shimizu, M. Isobe, S. Okamura, Y. Todo, H. Wang, H. F. Liu, J. Huang, X. Zhang, H. Liu, J. Cheng, C. J. Tang, and CFQS Team, *Nucl. Fusion* **61**, 036021 (2021).
- W. Horton, *Rev. Mod. Phys.* **71**, 735 (1999).
- V. Kornilov and R. Kleiber, *Phys. Plasmas* **11**, 3196 (2004).
- A. Zocco, G. G. Plunk, P. Xanthopoulos, and P. Helander, *Phys. Plasmas* **23**, 082516 (2016).
- A. Zocco, G. G. Plunk, and P. Xanthopoulos, *Phys. Plasmas* **27**, 022507 (2020).
- J. A. Baumgaertel, G. W. Hammett, D. R. Mikkelsen, M. Nunami, and P. Xanthopoulos, *Phys. Plasmas* **19**, 122306 (2012).
- H. E. Proll, P. Xanthopoulos, and P. Helander, *Phys. Plasmas* **20**, 122506 (2013).
- H. E. Proll, H. E. Mynick, P. Xanthopoulos, S. A. Lazerson, and B. J. Faber, *Plasma Phys. Controlled Fusion* **58**, 014006 (2016).
- T. H. Watanabe and H. Sugama, *Nucl. Fusion* **46**, 24 (2006).
- M. Nakata, M. Nunami, and H. Sugama, *Phys. Rev. Lett.* **118**, 165002 (2017).
- J. McKinney, M. J. Pueschel, B. J. Faber, C. C. Hegna, J. N. Talmadge, D. T. Anderson, H. E. Mynick, and P. Xanthopoulos, *J. Plasma Phys.* **85**, 905850503 (2019).
- T. M. Antonsen and B. Lane, *Phys. Fluids* **23**, 1205 (1980).
- M. Nakata, M. Honda, M. Yoshida, H. Urano, M. Nunami, S. Maeyama, T. H. Watanabe, and H. Sugama, *Nucl. Fusion* **56**, 086010 (2016).

- ²⁷A. Lenard and I. B. Bernstein, *Phys. Rev.* **112**, 1456 (1958).
- ²⁸M. Nakata, M. Nunami, H. Sugama, and T. H. Watanabe, *Plasma Phys. Controlled Fusion* **58**, 074008 (2016).
- ²⁹M. A. Beer, S. C. Cowley, and G. W. Hammett, *Phys. Plasmas* **2**, 2687 (1995).
- ³⁰S. P. Hirshman, W. I. van Rij, and P. Merkel, *Comput. Phys. Commun.* **43**, 143 (1986).
- ³¹A. Zocco, P. Xanthopoulos, H. Doerk, J. W. Connor, and P. Helander, *J. Plasma Phys.* **84**, 715840101 (2018).
- ³²M. Romanelli, C. Bourdelle, and W. Dorland, *Phys. Plasmas* **11**, 3845 (2004).
- ³³G. Rewoldt, Z. Lin, and Y. Idomura, *Comput. Phys. Commun.* **177**, 775 (2007).
- ³⁴J. A. Alcusón, P. Xanthopoulos, G. G. Plunk, P. Helander, F. Wilms, Y. Turkin, A. von Stechow, and O. Grulke, *Plasma Phys. Controlled Fusion* **62**, 035005 (2020).